J. Fluid Mech. (2022), *vol*. 941, R2, doi:10.1017/jfm.2022.268



Scaling laws for drag-to-thrust transition and propulsive performance in pitching flexible plates

Ze-Rui Peng[1,2], Yuehao Sun[1,2,3,†], Dan Yang[3,†], Yongliang Xiong[1,2], Lei Wang[3] and Lin Wang[1,2]

[1]Department of Mechanics, School of Aerospace Engineering, Huazhong University of Science and Technology, Wuhan 430074, PR China

[2]Hubei Key Laboratory for Engineering Structural Analysis and Safety Assessment, Wuhan 430074, PR China

[3]Department of Naval Architecture and Ocean Engineering, Huazhong University of Science and Technology, Wuhan 430074, PR China

(Received 27 September 2021; revised 2 December 2021; accepted 21 March 2022)

The propulsion of a pitching flexible plate in a uniform flow is investigated numerically. The effects of bending stiffness (K), pitching amplitude (A_L) and frequency (St) on the wake patterns, thrust generations and propulsive performances of the fluid–plate system are analysed. Four typical wake patterns, i.e. von Kármán, reversed von Kármán, deflected and chaotic wakes, emerge from various kinematics, and the $St - A_L$ wake maps are given for various K. The drag-to-thrust transitions (DTT) and the wake transitions (WT) between the von Kármán and reversed von Kármán wakes are examined. Results indicate that the WT and DTT boundaries can be scaled by the chord-averaged distance of travel, $\mathcal{L}$, which leads to $\mathcal{L} \times St \approx 1$ and $\mathcal{L} \times St \approx 1.2$, respectively. Further, the resonance mechanism for the performance enhancement is revealed and confirmed in a wide range of parameters. The dimensionless average speed of plate, $\mathcal{U}^*$ $(= \mathcal{L} \times St)$, is adopted merely to characterize the propulsive performances. For the first time, the $\mathcal{U}^*$-based scaling laws for the thrust and power are revealed in pitching rigid and flexible plates for various A_L and St. This study may deepen our understanding of biological swimming and flying, and provide a guide for bionic design.

Key words: flow–structure interactions, propulsion, swimming/flying

1. Introduction

Fish swimming and bird/insect flight, with 'their fascinating nature to appreciate, diversity to behold, and complications to comprehend' (Wu 2011), have aroused widespread interest

† Email addresses for correspondence: yhaosun@hust.edu.cn, dan_yang@hust.edu.cn

© The Author(s), 2022. Published by Cambridge University Press

https://doi.org/10.1017/jfm.2022.268 Published online by Cambridge University Press

in the research of interdisciplinary fields, e.g. biomechanics of animal locomotion and bionics, and stimulated innovative collaborations between scientists and engineers. Both flyers and swimmers in nature may utilize their oscillating appendages (wings and fins, here referred to as 'propellers') to generate thrust and/or lift as they propel themselves through fluids. Although the kinematics of biological propellers are typically complex, their essential features shared by various flyers and swimmers may be characterized by reasonably using some basic motion modes, involving pitching, heaving and their combinations. Thus, numerous theoretical (Nicholas & Moore 2014; Alon Tzezana & Breuer 2019), experimental (Anderson *et al.* 1998; Ramananarivo, Godoy-Diana & Thiria 2011) and numerical studies (Li & Lu 2012; Uddin, Huang & Sung 2015) have focused on the dynamics of the flapping foil/plate system, which provides an elegant and deft way for understanding the underlying principles in biological propulsion. Besides, the relevant research on the flapping-based locomotion also provided inspirations for developing innovative artificial biomimetic systems (Wu 2011).

A recent field of investigation on the flapping foil/plate systems concerns the thrust generation and its relation to wake pattern evolution, the major interrogation being about how to parameterize the drag-to-thrust transitions (DTT) and the wake transitions (WT) (Andersen *et al.* 2017; Lagopoulos, Weymouth & Ganapathisubramani 2019; Chao, Alam & Ji 2021). Although the inviscid theory predicts a DTT as the wake changes from the von Kármán wake to reversed von Kármán wake (von Kármán & Burgers 1935), the observations in experiments and simulations have revealed a lag between the WT and the DTT, due to the need to overcome the viscous and differential pressure resistance (Streitlien & Triantafyllou 1998; Andersen *et al.* 2017; Lagopoulos *et al.* 2019). For example, the study presented by Andersen *et al.* (2017) has shown that, for a flapping rigid foil in a two-dimensional flow, the WT occurs at $St_A = 0.18$, which precedes the DTT at $St_A = 0.28$. The amplitude-based Strouhal number $St_A = 2Af/U$, where U is the speed of uniform inflow, A and f are the flapping amplitude and frequency, respectively. Lagopoulos *et al.* (2019) further scaled the WT between the classical von Kármán wake and the reversed von Kármán wake for the flapping rigid foils with various kinematics, by introducing the chord-averaged trajectory length, $\mathcal{T}$. Results from the wake maps indicated that the onset of WT leads to $St_{\mathcal{T}} = \mathcal{T}f/U \to 1$, which offers a physical insight into the wake development. More recently, a numerical investigation carried out by Chao *et al.* (2021) indicated that the lag between DTT and WT exists in the pitching rigid foils with both symmetric and asymmetric oscillations.

Although invaluable insight into the basic aspects of flapping-based locomotion has been provided by investigations mentioned above, several issues are still open questions. One important and intriguing issue is about the passive role of wing/fin flexibility. In general, the biological wings and fins are flexible and often undergo a large passive deformation under the combined inertial, elastic and fluid forces. A variety of studies (Kang *et al.* 2011; Ramananarivo *et al.* 2011; Alben *et al.* 2012; Quinn, Lauder & Smits 2014; Zhu, He & Zhang 2014; Alon Tzezana & Breuer 2019) have indicated that the deformations affect many aspects of the flapping-based locomotion, including wake structures and propulsive performances. Beyond the above investigations on the rigid foil-flapping systems (Andersen *et al.* 2017; Lagopoulos *et al.* 2019; Chao *et al.* 2021), here we mainly aim to explore the effects of passive flexibility on the DTT/WT and propulsive characteristics for a flexible plate with the prescribed kinematics.

In the present study, we consider a particular version of flapping-based propulsion systems, in which the wings or fins are treated as a flexible plate with a negligible thickness, undergoing the forced harmonic pitching oscillation at the leading edge in a uniform oncoming flow. The influence of bending stiffness, pitching amplitude and

https://doi.org/10.1017/jfm.2022.268 Published online by Cambridge University Press

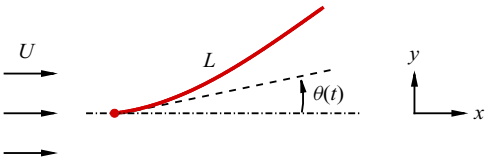


Figure 1. Schematic diagram for a pitching flexible plate. The plate with length L is immersed in a uniform inflow with speed U in the x-direction, and is forced to pitch around the leading edge with the pitching angle θ with respect to the free-stream direction. Here $\theta(t) = \theta_0 \cos 2\pi ft$, where θ_0 is the maximum pitching angle, and f is the frequency.

pitching frequency on the wake patterns, thrust generations and propulsive performances of the system have been systematically investigated. The resonance mechanism for the performance enhancement is revealed and confirmed in a wide range of parameters considered here. Further efforts are made to seek a universal metric for scaling not only the DTT/WT but also the propulsive performance, inspired by the work of Lagopoulos *et al.* (2019). The rest of the present paper is organized as follows. The physical problem and mathematical formulation are described in § 2. The numerical method and validation are presented in § 3. The result and discussion are given from a comprehensive numerical investigation in § 4. Finally, the concluding remarks are addressed in § 5.

2. Physical problem and mathematical formulation

The schematic diagram of a pitching flexible plate considered in the present study is shown in figure 1. The plate with length L is immersed in a uniform inflow with speed U in the x-direction, and pitches around the leading edge such that the pitching angle θ with respect to the free-stream direction varies with the simple harmonic motion

$$\theta(t) = \theta_0 \cos 2\pi ft, \tag{2.1}$$

where θ_0 is the maximum pitching angle, $\omega = 2\pi f$ is the angular frequency of oscillation. The leading edge of the flexible plate is fixed, and the other part can move freely and deform passively due to the flow–structure interactions.

In this system, the fluid flow is governed by the incompressible Navier–Stokes equations

$$\frac{\partial \boldsymbol{v}}{\partial t} + \boldsymbol{v} \cdot \nabla \boldsymbol{v} = -\frac{1}{\rho}\nabla p + \frac{\mu}{\rho}\nabla^2 \boldsymbol{v} + \boldsymbol{f}_b, \tag{2.2}$$

$$\nabla \cdot \boldsymbol{v} = 0, \tag{2.3}$$

where $\boldsymbol{v} = (u, v)$ is the velocity, p is the pressure, ρ is the density of the fluid, μ is the dynamic viscosity and $\boldsymbol{f}_b$ is the body force term. A uniform velocity U is set at the inlet boundary and the side boundaries of the fluid computational domain. A Neumann condition is specified at the outlet boundary. The deformation and motion of the flexible plate are described by the structural equation (Hua, Zhu & Lu 2013)

$$\rho_s h \frac{\partial^2 \boldsymbol{X}}{\partial t^2} - Eh \frac{\partial}{\partial s}\left[\left(1 - \left|\frac{\partial \boldsymbol{X}}{\partial s}\right|^{-1}\right)\frac{\partial \boldsymbol{X}}{\partial s}\right] + EI\frac{\partial^4 \boldsymbol{X}}{\partial^4 s} = \boldsymbol{F}_s, \tag{2.4}$$

where s is the Lagrangian coordinate along the flexible plate, h is the structure thickness, $\boldsymbol{X}(s, t) = (X(s, t), Y(s, t))$ is the position vector of the plate, $\boldsymbol{F}_s = (F_x, F_y)$ is the Lagrangian force exerted on the plate by the surrounding fluid, and ρ_s is the structural density. Here Eh and EI are the structural stretching and bending rigidity, respectively.

https://doi.org/10.1017/jfm.2022.268 Published online by Cambridge University Press

For the structural equation, the boundary condition at the leading edge of the plate is $\boldsymbol{X}(t) = (0, 0)$, $\partial \boldsymbol{X}/\partial s = (\cos\theta, \sin\theta)$, and the boundary condition at the free end of the plate is $-Eh(1 - |\partial \boldsymbol{X}/\partial s|^{-1})\partial \boldsymbol{X}/\partial s + EI\partial^3 \boldsymbol{X}/\partial^3 s = 0$, $\partial^2 \boldsymbol{X}/\partial s^2 = 0$.

The characteristic quantities, ρ, L and U, are chosen to normalize the above equations. Thus the following dimensionless governing parameters are introduced: the Reynolds number $Re = \rho UL/\mu$, the flapping amplitude $A_L = 2A/L = 2\sin\theta_0$ (where A is dimensional semi-amplitude of the trailing edge without considering the plate's passive deformation), the L-based Strouhal number (or reduced frequency) $St = Lf/U$, the stretching stiffness $S = Eh/(\rho U^2 L)$, the bending stiffness $K = EI/(\rho U^2 L^3)$, the mass ratio of the plates and the fluid $M = \rho_s h/(\rho L)$. Moreover, the relevant parameters, including the thrust coefficient (C_T) and the power coefficient (C_P), are introduced to evaluate the performance of the pitching plate, and defined respectively as

$$C_T = \frac{T}{0.5\rho U^2 L} = \frac{-\langle F_x(s,t)\rangle}{0.5\rho U^2 L} \quad \text{and} \quad C_p = \frac{P}{0.5\rho U^3 L} = \frac{\langle -\boldsymbol{F}_s(s,t)\cdot\partial_t \boldsymbol{X}(s,t)\rangle}{0.5\rho U^3 L}, \tag{2.5a,b}$$

where T is the cycle-averaged net thrust for the overall plate, i.e. $T = -\langle F_x(s,t)\rangle$, P is the cycle-averaged power for the overall plate, i.e. $P = \langle -\boldsymbol{F}_s(s,t)\cdot\partial_t \boldsymbol{X}(s,t)\rangle$, and $\langle\cdot\rangle := (1/T_f)\int_{t_0}^{t_0+T_f}\int_0^1 (\cdot)\,\mathrm{d}s\,\mathrm{d}t$ (T_f is flapping period, i.e. $T_f = 1/f$, and t_0 is the instant when the periodicity is reached, e.g. $t_0 = 20T_f$ for most cases).

3. Numerical method and validation

The Navier–Stokes equations are solved numerically by the lattice Boltzmann method (Chen & Doolen 1998), and the structure equation (2.4) is discretized by a nonlinear finite element method with the co-rotational scheme (Doyle 2001). The immersed boundary method is applied to treat flow–structure interaction (Peskin 2002). The body force term $\boldsymbol{f}_b$ in (2.2) represents an interaction force between the fluid and the immersed boundary to enforce the no-slip velocity boundary condition. A detailed description of the numerical method can be found in our previous papers (Peng, Huang & Lu 2018*a*).

Based on our convergence studies with different computational domains, the computational domain for fluid flow is chosen as $50L \times 30L$ in the x- and y-directions. The domain is large enough so that the blocking effects of the boundaries are not significant. According to independence studies for the grid spacing and time step, in the x- and y-directions, the mesh is uniform with spacing $\Delta x = \Delta y = L/100$. The flexible plate is discretized with a mesh size of $\Delta s = L/100$. The time step is $\Delta t = T_f/10\,000$ for the simulations of fluid flow and plate motion, with $T_f = 1/f$ being the flapping period. The numerical strategy used in this study has been validated in our previous numerical investigations on the self-propulsion of flapping flexible plates, and a detailed numerical validation can be found in the previous papers (Hua *et al.* 2013; Peng *et al.* 2018*a*; Peng, Huang & Lu 2018*b*). Besides, the numerical strategy has also been successfully applied to a wide range of flows, such as the dynamics of a three-dimensional circular flexible plate in a uniform flow (Hua, Zhu & Lu 2014).

4. Results and discussion

In the study, the effects of bending stiffness ($1 < K < 10^3$), flapping amplitude ($0.4 \le A_L \le 1.2$) and Strouhal number ($0.2 \le St \le 1.2$) on the WT/DTT and propulsive performances of the system are investigated. It is noted that the rigid plate cases with

https://doi.org/10.1017/jfm.2022.268 Published online by Cambridge University Press

the corresponding parameters are also simulated for comparisons. In all our simulations, the Reynolds number, mass ratio and stretching stiffness are fixed at $Re = 240$, $M = 1$ and $S = 1000$, respectively. The S is chosen as a large value so that the stretching deformation of the plate can be neglected. The Reynolds number, which lies in a moderate range with a significant viscous effect, is representative of the insect flight (Michelin & Smith 2009) or swimming of small animals, e.g. tadpole and zebrafish larvae (Gazzola, Argentina & Mahadevan 2014). Here $M = 1$ matches with $M \sim O(1)$ for the case of a flexible flapping plate in the air, which is a representative value for the wing of an insect, such as dragonfly (Jongerius & Lentink 2010).

4.1. *Wake patterns and the thrust generations*

In this section, we analyse the wake patterns and thrust generations in the $St - A_L$ plane for various K. Based on a variety of simulations for a wide range of parameters considered here, we have identified four typical wake patterns emerging from various kinematics, i.e. von Kármán, reversed von Kármán, deflected and chaotic wakes. Animated visualisations of the typical wake patterns have also been provided in supplementary movies available at https://doi.org/10.1017/jfm.2022.268. Figure 2(*a*) shows the instantaneous vorticity contour for the rigid case with $St = 0.6, A_L = 0.2$, corresponding to the von Kármán wake. It is seen that the shear layer with positive (or negative) vorticity on the lower (upper) surface of the plate begins to separate near the trailing edge. And it rolls up to form a pair of alternately shedding vortices, which convect downstream parallel to the centre line as two rows of vortices having opposite rotation in the far wake (see figure 2*a*). Figure 2(*b*) illustrates the development and spatial organization of the reversed von Kármán for the rigid case with $St = 0.6, A_L = 0.6$. In contrast to the von Kármán wake, the vortices with anticlockwise or clockwise rotation are located above or below the centre line, respectively. The vortices in this configuration may induce a backward jet in the wake, which can be considered a prognosticator of thrust generation. The instantaneous vorticity contour for the rigid case with $St = 1.0, A_L = 0.6$, corresponding to the deflected wake, is shown in figure 2(*c*). As one can see, a series of counter-rotating vortex pairs align with each other and travel downstream with a deflection angle with respect to the free-stream direction. The distance between cores of counter-rotating vortices in the vortex pair is very small, so that a stronger propulsive jet may be induced by the vortex pair according to the Biot–Savart law (Habibah & Fukumoto 2017). Besides, for the case with higher St and A_L, e.g. $St = 1.2, A_L = 1.2$ and $K = 50$, a chaotic vortical structure may be found in the wake of the pitching plate, as shown in figure 2(*d*). Moreover, it is worth noting that the four typical wake patterns in our simulations are ubiquitous in the flapping foil/plate systems, which are consistent with the observations in literature (Hua *et al.* 2013; Zhu *et al.* 2014; Andersen *et al.* 2017; Lagopoulos *et al.* 2019; Chao *et al.* 2021).

Figure 3 shows the phase diagrams for the four typical wake patterns in the $St - A_L$ plane for the pitching plates with various flexibility. The rigid plate scenarios ($K = \infty$) are also shown in figure 3(*f*) for comparisons. It is illustrated clearly that a similar WT occurs for all the rigid and flexible cases, especially, as the increase of A_L and St (from the bottom left to top right in the phase diagrams), the von Kármán, reversed von Kármán, deflected and chaotic wakes are observed in succession. All the cases with the von Kármán wake exist within the drag-producing regime, while cases with the deflected or chaotic wake exist within the thrust-producing regime. Compared to the rigid-plate scenario as shown in figure 3(*f*), the proper flexibility of the plate may inhibit the drag-producing wake and trigger the transitions to the propulsive-producing wake for the identical kinematics (e.g. figure 3*b*,*c*). The best-fit curves (where the net thrust is zero) are denoted in the $St - A_L$

https://doi.org/10.1017/jfm.2022.268 Published online by Cambridge University Press

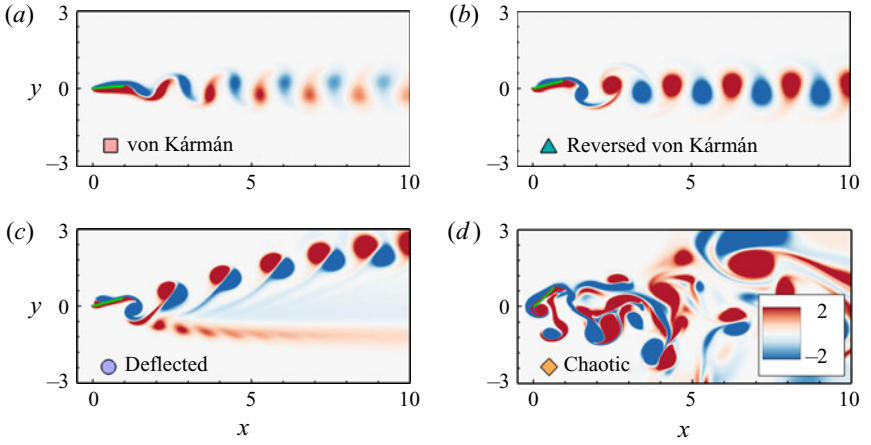


Figure 2. The instantaneous vorticity contours for the four typical wake patterns of the pitching plate: (*a*) von Kármán ($St = 0.6$, $A_L = 0.2$ and $K = \infty$), (*b*) reversed von Kármán ($St = 0.6$, $A_L = 0.6$ and $K = \infty$), (*c*) deflected ($St = 1$, $A_L = 0.6$ and $K = \infty$) and (*d*) chaotic wakes ($St = 1.2$, $A_L = 1.2$ and $K = 50$).

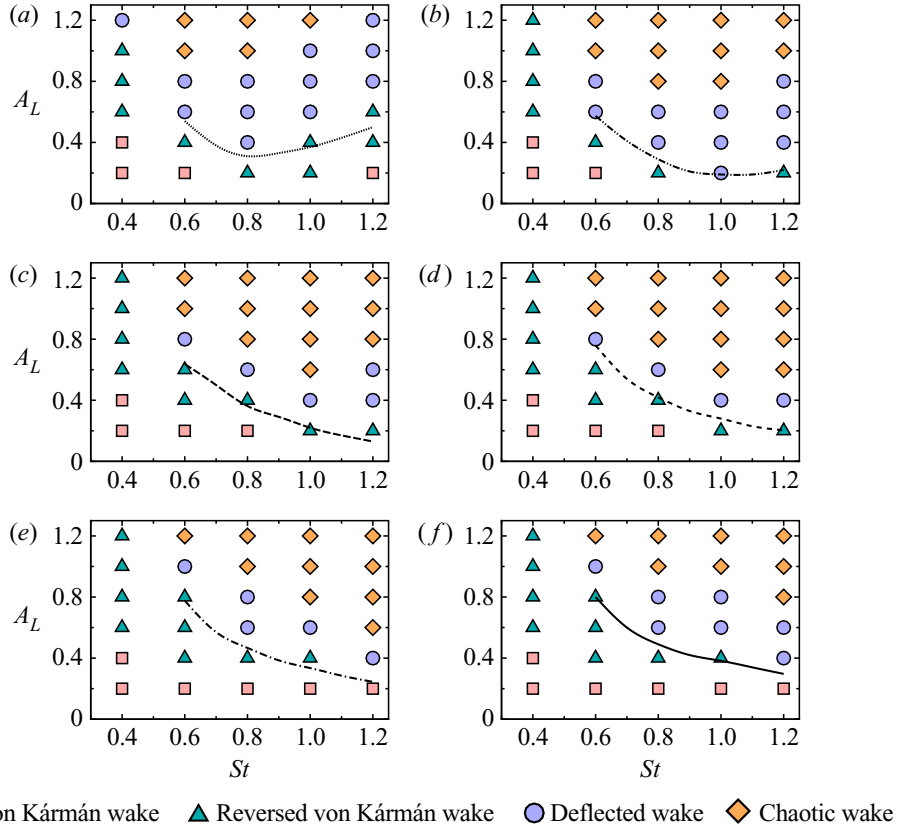


Figure 3. Overview of the four typical wake pattern regions on the $St - A_L$ plane for the pitching plate with $K = 3$ (*a*), 5 (*b*), 10 (*c*), 20 (*d*), 50 (*e*) and ∞ (*f*). The symbols □, △, ○, and ◇ represent the von Kármán, reversed von Kármán, deflected and chaotic wakes, respectively. The black best-fit curves show the DTT for various K.

https://doi.org/10.1017/jfm.2022.268 Published online by Cambridge University Press

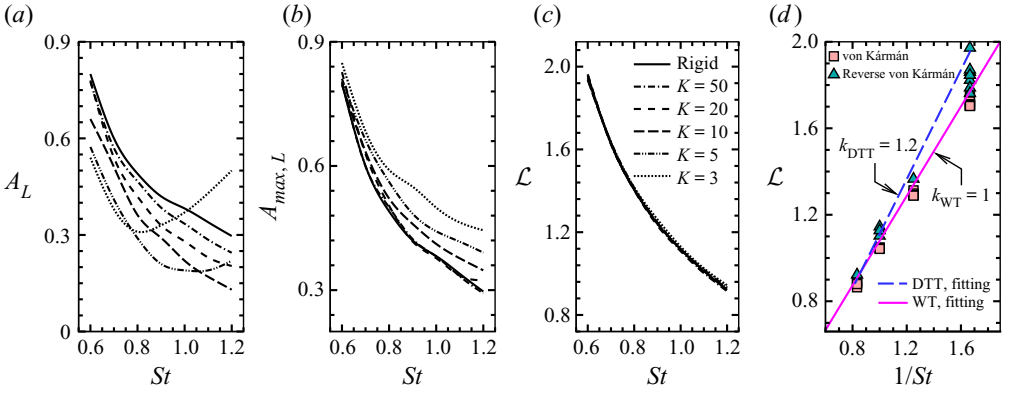


Figure 4. The best-fit curves for DTT with various K in the $St - A_L$ (a), $St - A_{max,L}$ (b), $St - \mathcal{L}$ (c) and $1/St - \mathcal{L}$ (d) phase planes. Here, $A_{max,L}$ and A_L ($= 2A/L = 2\sin\theta$) are the L-normalized pick-to-pick trailing amplitudes with and without considering the plate's passive deformation, respectively. The fitting line for the transitions between the von Kármán wakes and the reversed von Kármán wakes is also plotted in the $1/St - \mathcal{L}$ plane. The fit lines are described by $\mathcal{L} = k \times St^{-1} + b$, where $k = k_{WT} = 1$, $b = 0.046$ for the wake transition (WT), and $k = k_{DTT} = 1.2$, $b = 0.09$ for the DTT, respectively.

plane (see figure 3), showing the DTT for various K. It is clear that a lag exists between the WT and the DTT because a weak propulsive wake cannot overcome profile drag or velocity fluctuations and pressure difference within the control volume (Lagopoulos *et al.* 2019). This observation is in agreement with previous measurements and simulations for the flapping rigid foils (Andersen *et al.* 2017; Lagopoulos *et al.* 2019; Chao *et al.* 2021), but it is confirmed for the first time in the flexible-plate scenarios, according to our simulations.

4.2. *Scaling laws for the wake and drag-to-thrust transitions*

The best-fit curves for DTT in figure 3 are reproduced in figure 4(a). It is shown that for both rigid and flexible cases, the thrust can only be produced if the plate performs an oscillation with sufficiently high St and A_L. Moreover, it can be generally believed that the passive flexibility allows the plate to achieve the thrust with a smaller pitching amplitude or frequency; the optimal stiffness for the emergence of thrust is in the moderate range of 5–10. However, it should be noted that the excessive flexibility may inhibit the onset of thrust under the high pitching frequencies, e.g. the cases with $K = 3$ and $St > 1$ (see figure 4a). Moreover, figure 4(b) shows the boundaries for the DTT with various K in the $St - A_{max,L}$ plane, where $A_{max,L} = A_{max}/L$ is the L-normalized pick-to-pick trailing amplitude. As shown in figure 4(a,b), the curves in the $St - A_L$ and $St - A_{max,L}$ planes do not overlap each other, which indicates that DTT cannot be described merely by the combination of St and A_L (or $A_{max,L}$), i.e. $St_A = A_L \times St = 2Af/U$ (or $St_{A_{max}} = A_{max,L} \times St = A_{max}f/U$). Also, we note that the WT for the flexible pitching plates can not be characterized by the amplitude-based Strouhal numbers, e.g. St_A or $St_{A_{max}}$ (not shown in figure 4). This conclusion is also consistent with those for rigid foils in literature. According to Andersen *et al.* (2017) and Lagopoulos *et al.* (2019), St_A cannot be regarded as an expression of self-similarity for the drag-to-thrust wake transitions, which not only depends on the frequency and the trailing amplitude, but also depends sensitively on other details of the kinematics.

https://doi.org/10.1017/jfm.2022.268 Published online by Cambridge University Press

The dimensionless chord-averaged distance of travel per cycle, $\mathcal{L}$, is introduced by Lagopoulos *et al.* (2019) to characterize the quantity of fluid displaced and scale the transition boundaries between the von Kármán and reversed von Kármán wakes in flapping rigid foils. In their study, $\mathcal{L}$ is defined as

$$\mathcal{L} = \frac{1}{L}\int_0^1 \int_0^{1/f} \sqrt{\dot{X}^2(s,t) + \dot{Y}^2(s,t)}\,\mathrm{d}t\,\mathrm{d}s, \tag{4.1}$$

where $\dot{X}$ is the horizontal velocity of the plate relative to the oncoming flow. By definition, it is reasonably believed that $\mathcal{L}$ is directly related to the thrust of the plate, which is generated by displacing and accelerating fluid. Thus, the curves in figure 4(*a*) are redrawn in the $St - \mathcal{L}$ phase plane in figure 4(*c*), showing a remarkable collapse of all the curves corresponding to the DTT for various K. By fitting the overlapping curves in figure 4(*c*), the boundaries of DTT for various K can be expressed as a unified formula, i.e. $\mathcal{L} = k_{DTT} \times St^{-1} + b$, where $k_{DTT} = 1.2$, $b = 0.046$ (see dashed line in figure 4*d*), which leads to $\mathcal{L} \times St \approx 1.2$. The fitting line for the transition boundaries between the von Kármán wakes and the reversed von Kármán wakes is also plotted in the $1/St - \mathcal{L}$ plane (see solid line in figure 4*d*). The fitting result for the wake transitions (WT) leads to $\mathcal{L} \times St \approx 1$. Combining the recent (Lagopoulos *et al.* 2019) and current studies, we note that $\mathcal{L} \times St \to 1$, as a prognosticator of WT, is valid not only for rigid flapping foils but also for flexible scenarios. Further, as a result of $(\mathcal{L} \times St)_{DTT} > (\mathcal{L} \times St)_{WT}$, the WT occur earlier than the DTT, especially in the low St region (figure 4*d*).

4.3. *Resonances and the propulsive performances*

Figure 5(*a–c*) show A_{tip} (the maximum transverse displacement of the trailing edge), C_T, and C_P vs K for $A_L = 0.2$ and various St, respectively. For each St, the peaks in performance parameters, e.g. A_{tip}, C_T and C_p, are achieved at the same time at an optimal K that increases with the increase of St. It is noted that the system is supposed to operate in resonance when A_{tip} reaches a local maximum at the optimal K (Alon Tzezana & Breuer 2019). To analyse the resonance responses of the plate, the frequency ratio, $\omega^* = 2\pi f/\omega_1^{fluid}$, is introduced. Here following the theory proposed by Van Eysden & Sader (2006), the first natural frequency of the plate in a fluid is given as

$$\omega_1^{fluid} = \omega_1^{vac}\left[1 + \frac{\pi\epsilon}{4C_1 M} \times \Gamma_f(\epsilon)\right]^{-1/2}, \tag{4.2}$$

where $\omega_1^{vac} = (C_1^2 U/L)(\sqrt{K/M})$ is the first natural frequency in vacuum, $C_1 = 1.875$ and $\Gamma_f(\epsilon)$ is hydrodynamic function (Van Eysden & Sader 2006). Thus the frequency ratio can be calculated as

$$\omega^* = \frac{2\pi St}{C_1^2}\sqrt{\frac{M}{K}}\left[1 + \frac{\pi\epsilon}{4C_1 M} \times \Gamma_f(\epsilon)\right]^{1/2}. \tag{4.3}$$

The variations of A_{tip}, C_T and C_p in figure 5(*a–c*) are reproduced in figure 5(*d–f*) as a function of ω^*. It is seen that the peaks in performance parameters for varying St overlap at $\omega^* \approx 1.1$, illustrating the optimal performance is achieved at the same time with the onset of structural resonance when pitching frequency ω is close to ω^{fluid}. However, it is worth noting that, as the increase of A_L (see figure 5*d*,*g*,*j*), the value of ω^* at the resonance gradually decreases and deviates from 1. This is because the theoretical formula, which is established under the assumption of small-amplitude vibrations, overestimates the actual

https://doi.org/10.1017/jfm.2022.268 Published online by Cambridge University Press

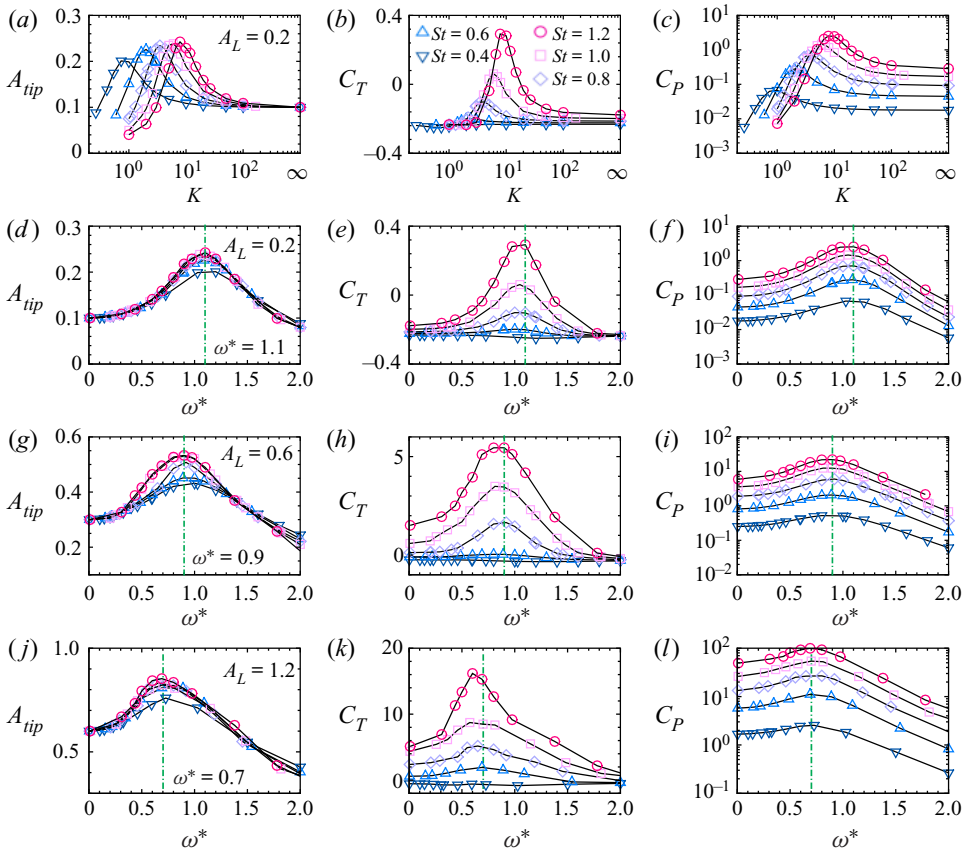


Figure 5. Dynamical performance of the pitching flexible plate in a flow: the maximum transverse displacement of the trailing edge, A_{tip} (*a*,*d*,*g*,*j*), the thrust coefficient, C_T (*b*,*e*,*h*,*k*), and the power coefficient, C_P (*c*,*f*,*i*,*l*), as a function of K for $A_L = 0.2$ (*a*–*c*), or as a function of ω^* for $A_L = 0.2$ (*d*–*f*), 0.6 (*g*–*i*), 1.2 (*j*–*l*), respectively.

value of ω_1^{fluid} for high A_L cases. Specifically, as pitching amplitude increases, the added mass (M_{add}) would increase further, which results in the decrease of the actual ω_1^{fluid} for the plate due to $\omega_1^{fluid} \sim (M + M_{add})^{-1/2}$ (Alon Tzezana & Breuer 2019). In other words, the overestimated value of ω_1^{fluid} by the theoretical formula above, in turn, leads to ω^* at the resonance being much less than 1 for the high A_L cases, e.g. $\omega^* = 0.7$ for $A_L = 1.2$ (see figure 5*j*). The above results have confirmed the resonance mechanism that may improve the propulsive performance through properly adjusting the passive flexibility or flapping frequency of the plate, which is consistent with the previous studies (Kang *et al.* 2011; Alon Tzezana & Breuer 2019). It is noted that several literature has reported that the propulsive performances may be maximized for the frequency ratios considerably lower than unity (Kang *et al.* 2011; Ramananarivo *et al.* 2011), and this may be because that ω_1^{vac}, instead of ω_1^{fluid}, was used to scale flapping frequency, which leads to a much lower ω^* at the resonance.

https://doi.org/10.1017/jfm.2022.268 Published online by Cambridge University Press

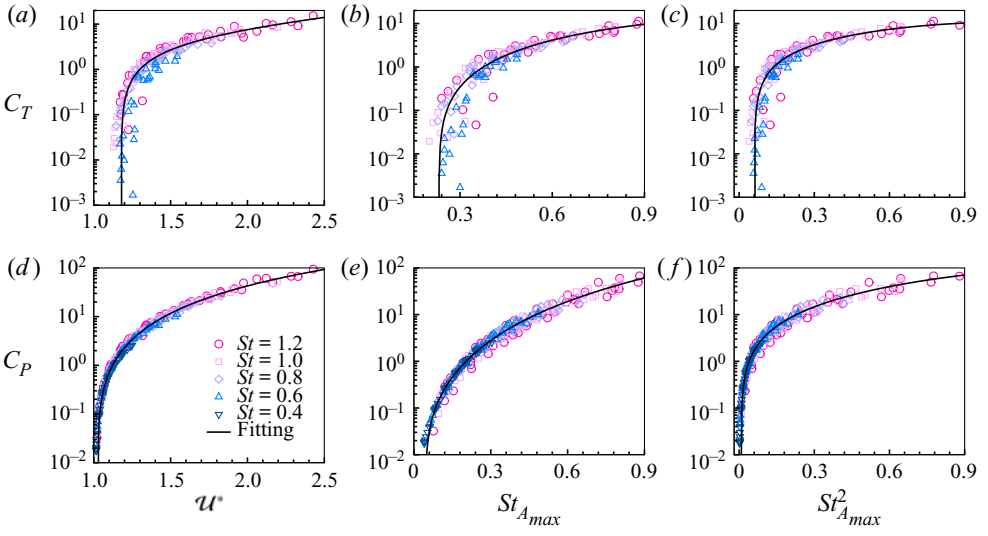


Figure 6. The thrust (*a–c*) and power (*d–f*) coefficients as a function of $\mathcal{U}^*(= St \cdot \mathcal{L})$ (*a*,*d*), $St_{A_{max}}$ (*b*,*e*) and $St^2_{A_{max}}$ (*c*,*f*).

4.4. *Scaling laws for the propulsive performances*

According to the definition of $\mathcal{L}$ in § 4.2, we have

$$St \times \mathcal{L} = \frac{fL}{U} \times \frac{\mathcal{U} \times T_f}{L} = \frac{\mathcal{U}}{U}, \tag{4.4}$$

where $\mathcal{U}$ is time–space average speed of the plate. Thus, the product $St \times \mathcal{L}$ has a clear physical interpretation, that is, the dimensionless average speed of the plate, denoted as $\mathcal{U}^*$. Fundamentally, the plate generates the thrust by displacing and accelerating fluid out of its path. The quantity of fluid displaced and accelerated by the plate is dependent on the path length travelled by the plate over one period of oscillation, which is evaluated by $\mathcal{L}$ (Lagopoulos *et al.* 2019). And then, the product $\mathcal{U}^* = St \times \mathcal{L}$ can be used to scale the cycle-averaged thrust. All the data of C_T and C_P in figure 5 are plotted again in figures 6(*a*) and 6(*d*), respectively, as functions of $\mathcal{U}^*$. As one can see, all the symbols, corresponding to the cases with varying bending stiffness (K) and kinematics parameters (A_L and St), collapse together onto a single curve for C_T and C_P, respectively.

Moreover, the previous experiments and theory agree that the thrust performance depends on the transverse velocity of tail motion for pitching and heaving foils, leading to $St_{A_{max}}$-based metrics as typical arguments for describing the performance in aquatic swimming (Smits 2019). As shown in figure 6(*b*,*e*), the thrust and power data collapse well onto a single curve, suggesting that $St_{A_{max}}$ can be used for scaling the C_T and C_P of the pitching plates. Further, by doing a simple scaling analysis (Dewey *et al.* 2013; Quinn, Lauder & Smits 2015), the thrust generated by a pitching motion depends on the square of transverse tail velocity, resulting in $C_T \sim St^2_{A_{max}}$. This scaling law is also in accord with the conclusions drawn from slender body theory (Lighthill 1960; Akbarzadeh & Borazjani 2019; Smits 2019). According to Akbarzadeh & Borazjani (2019), the thrust generated by a backward travelling wave over a plate is scaled with $St^2_{A_{max}}(1 - (U^2/C^2))$, where $C = f\lambda$ is the wave speed and λ is the wavelength. Our numerical results indicate that the pitching plates may approximately deform and move in the form of travelling waves with C being much larger than U, which leads to $C_T \sim St^2_{A_{max}}(1 - (U^2/C^2)) \approx St^2_{A_{max}}$.

https://doi.org/10.1017/jfm.2022.268 Published online by Cambridge University Press

This conclusion also suggests that the thrust generation is dominated by the transverse velocity rather than the wave speed for the pitching plates considered in the present study. Plotting the thrust and power data as a function of $St^2_{A_{max}}$ yields figure 6(c,f). The scaling demonstrates remarkable collapses which is similar to the $\mathcal{U}^*$-based scaling. The results also show the spread in data within the low-thrust region is slightly less than that using $St_{A_{max}}$ (see figure 6b).

It is not surprising that the $\mathcal{U}^*$-based and $St_{A_{max}}$-based scales demonstrate a similar goodness of fit for the performance data. Both metrics focus on characterising added mass effect, which dominates the mean thrust generated by the pitching motions, according to Floryan *et al.* (2017). We also note that the two arguments neglect the drag on the propulsor, thus the scaling laws based on them will be only held when the drag is small relative to the total thrust (Smits 2019). Further, compared with the $St_{A_{max}}$-based metrics, $\mathcal{U}^*$ cannot be derived from a linearized theory although it has a clear physical interpretation mentioned above; meanwhile, it requires more information on the plate than $St_{A_{max}}$, which may cause measurement difficulty in applications. Whereas, due to including more details of the kinematics, $\mathcal{U}^*$ is able to serve as a universal scale to not only characterise the performance of propulsion, but also capture the DTT/WT, suggesting its fundamental role in revealing the dynamics of flapping-based propulsion. We also note that these scaling laws are applicable for various flows in a wide range of the parameters considered in the present study.

5. Concluding remarks

In summary, we carried out a numerical investigation on the dynamics of a pitching flexible plate in a uniform flow. The effects of K, A_L and St on the wake patterns, thrust generations and propulsive performances of the fluid–plate system were analysed. We have identified four typical wake patterns emerging from various kinematics, i.e. von Kármán, reversed von Kármán, deflected and chaotic wakes. The phase diagrams for the four wake patterns in the $St - A_L$ plane were given for various K. The boundaries of WT and DTT were examined for both rigid and flexible plates. Results have indicated that the WT and DTT boundaries can be scaled by the dimensionless parameter, $\mathcal{L}$, which leads to $\mathcal{U}^* = \mathcal{L} \times St \approx 1$ and $\mathcal{U}^* \approx 1.2$, respectively. A lag between the WT and DTT was observed for the flexible plate, which is consistent with previous measurements and simulations for rigid cases. It was found that the peaks in C_T and C_P are achieved when ω is closed to ω_1^{fluid}, at which the system operates in resonance. As the pitching amplitude increases, ω_1^{fluid} would decrease due to the enhancement of the added mass. Further, it was indicated that propulsive characteristics of this fluid–plate system could be merely described by one physical quantity, $\mathcal{U}^*$. For the first time, these simple scaling laws for C_T and C_P are revealed in both rigid and flexible pitching plates. We also note that these scaling laws are tenable for various flow patterns in a wide range of the parameters considered in our two-dimensional simulations. However, the universality of $\mathcal{U}^*$-based metric should be further evaluated in the more general situations where the more complex kinematics and three-dimensional shape effects should be considered. This is beyond the scope of the present paper but will be a focus of our future research.

Supplementary movies. Supplementary movies are available at https://doi.org/10.1017/jfm.2022.268.

Acknowledgements. The authors would like to thank Mr Y. Lu for valuable discussions on topics related to this work.

https://doi.org/10.1017/jfm.2022.268 Published online by Cambridge University Press

Funding. This work was supported by the Natural Science Foundation of China (grant number 11902120).

Declaration of interests. The authors report no conflict of interest.

Author ORCIDs.
Ze-Rui Peng https://orcid.org/0000-0002-5717-3901;
Yongliang Xiong https://orcid.org/0000-0002-2567-1922.

References

Akbarzadeh, A.M. & Borazjani, I. 2019 Reducing flow separation of an inclined plate via travelling waves. *J. Fluid Mech.* **880**, 831–863.

Alben, S., Witt, C., Baker, T.V., Anderson, E. & Lauder, G.V. 2012 Dynamics of freely swimming flexible foils. *Phys. Fluids* **24**, 051901.

Alon Tzezana, G. & Breuer, K.S. 2019 Thrust, drag and wake structure in flapping compliant membrane wings. *J. Fluid Mech.* **862**, 871–888.

Andersen, A., Bohr, T., Schnipper, T. & Walther, J.H. 2017 Wake structure and thrust generation of a flapping foil in two-dimensional flow. *J. Fluid Mech.* **812**, R4.

Anderson, J.M., Streitlien, K., Barrett, D.S. & Triantafyllou, M.S. 1998 Oscillating foils of high propulsive efficiency. *J. Fluid Mech.* **360**, 41–72.

Chao, L.-M., Alam, M.M. & Ji, C. 2021 Drag–thrust transition and wake structures of a pitching foil undergoing asymmetric oscillation. *J. Fluids Struct.* **103**, 103289.

Chen, S. & Doolen, G.D. 1998 Lattice Boltzmann method for fluid flows. *Annu. Rev. Fluid Mech.* **30**, 329–364.

Dewey, P.A., Boschitsch, B.M., Moored, K.W., Stone, H.A. & Smits, A.J. 2013 Scaling laws for the thrust production of flexible pitching panels. *J. Fluid Mech.* **732**, 29–46.

Doyle, J.F. 2001 *Nonlinear Analysis of Thin-Walled Structures: Statics, Dynamics, and Stability*. Springer.

Floryan, D., Van Buren, T., Rowley, C.W. & Smits, A.J. 2017 Scaling the propulsive performance of heaving and pitching foils. *J. Fluid Mech.* **822**, 386–397.

Gazzola, M., Argentina, M. & Mahadevan, L. 2014 Scaling macroscopic aquatic locomotion. *Nat. Phys.* **10**, 758–761.

Habibah, U. & Fukumoto, Y. 2017 A counter-rotating vortex pair in inviscid fluid. *AIP Conf. Proc.* **1913** (1), 020022.

Hua, R.-N., Zhu, L. & Lu, X.-Y. 2013 Locomotion of a flapping flexible plate. *Phys. Fluids* **25**, 121901.

Hua, R.-N., Zhu, L. & Lu, X.-Y. 2014 Dynamics of fluid flow over a circular flexible plate. *J. Fluid Mech.* **759**, 56–72.

Jongerius, S.R. & Lentink, D. 2010 Structural analysis of a dragonfly wing. *Exp. Mech.* **50**, 1323–1334.

Kang, C.-K., Aono, H., Cesnik, C.E.S. & Shyy, W. 2011 Effects of flexibility on the aerodynamic performance of flapping wings. *J. Fluid Mech.* **689**, 32–74.

von Kármán, T. & Burgers, J.M. 1935 General aerodynamic theory-perfect fluids. In *Aerodynamic theory II* (ed. W.F. Durand). Dover.

Lagopoulos, N., Weymouth, G. & Ganapathisubramani, B. 2019 Universal scaling law for drag-to-thrust wake transition in flapping foils. *J. Fluid Mech.* **872**, R1.

Li, G.-J. & Lu, X.-Y. 2012 Force and power of flapping plates in a fluid. *J. Fluid Mech.* **712**, 598–613.

Lighthill, M.J. 1960 Note on the swimming of slender fish. *J. Fluid Mech.* **9**, 305–317.

Michelin, S. & Smith, S.G.L. 2009 Resonance and propulsion performance of a heaving flexible wing. *Phys. Fluids* **21**, 071902.

Nicholas, M. & Moore, J. 2014 Analytical results on the role of flexibility in flapping propulsion. *J. Fluid Mech.* **757**, 599–612.

Peng, Z.-R., Huang, H. & Lu, X.-Y. 2018*a* Collective locomotion of two closely spaced self-propelled flapping plates. *J. Fluid Mech.* **849**, 1068–1095.

Peng, Z.-R., Huang, H. & Lu, X.-Y. 2018*b* Hydrodynamic schooling of multiple self-propelled flapping plates. *J. Fluid Mech.* **853**, 587–600.

Peskin, C.S. 2002 The immersed boundary method. *Acta Numer.* **11**, 479–517.

Quinn, D.B., Lauder, G.V. & Smits, A.J. 2014 Scaling the propulsive performance of heaving flexible panels. *J. Fluid Mech.* **738**, 250–267.

Quinn, D.B., Lauder, G.V. & Smits, A.J. 2015 Maximizing the efficiency of a flexible propulsor using experimental optimization. *J. Fluid Mech.* **767**, 430–448.

https://doi.org/10.1017/jfm.2022.268 Published online by Cambridge University Press

RAMANANARIVO, S., GODOY-DIANA, R. & THIRIA, B. 2011 Rather than resonance, flapping wing flyers may play on aerodynamics to improve performance. *Proc. Natl Acad. Sci. USA* **108**, 5964–5969.

SMITS, A.J. 2019 Undulatory and oscillatory swimming. *J. Fluid Mech.* **874**, P1.

STREITLIEN, K. & TRIANTAFYLLOU, G.S. 1998 On thrust estimates for flapping foils. *J. Fluids Struct.* **12** (1), 47–55.

UDDIN, E., HUANG, W.-X. & SUNG, H.J. 2015 Actively flapping tandem flexible flags in a viscous flow. *J. Fluid Mech.* **780**, 120–142.

VAN EYSDEN, C.A. & SADER, J.E. 2006 Resonant frequencies of a rectangular cantilever beam immersed in a fluid. *J. Appl. Phys.* **100** (11), 114916.

WU, T.Y. 2011 Fish swimming and bird/insect flight. *Annu. Rev. Fluid Mech.* **43** (1), 25–58.

ZHU, X., HE, G. & ZHANG, X. 2014 How flexibility affects the wake symmetry properties of a self-propelled plunging foil. *J. Fluid Mech.* **751**, 164–183.

https://doi.org/10.1017/jfm.2022.268 Published online by Cambridge University Press